

Fabrication of Transparent and Electroconductive Scaffolds for Neural Stem Cell Culture Combining 3D Printing and Conjugated Polymers

Alexandre Ribeiro

Master Student in Biomedical Engineering, Instituto Superior Técnico, Universidade de Lisboa, Av. Rovisco Pais, 1049-001 Lisboa, Portugal

Transparent, electroconductive scaffolds were developed to establish platforms to study the effect of electric field on neural stem cells (NSC) expansion and differentiation: the first fabricated through the extrusion of commercial filaments; the second from poly(ethylene glycol) diacrylate (PEGDA) hydrogel and inkjet printing of the conjugated polymer poly(3,4-ethylenedioxythiophene):poly(styrene sulfonate) (PEDOT:PSS). Both scaffolds present adequate conductivity to work in the current range explored in literature. While PEGDA hydrogel-based scaffolds present suitable transparency for optical microscopy, optimization of the transparency of 3D extruded scaffolds is needed. NSCs expanded on scaffolds under electrical stimulation showed increased elongation and alignment according to electric field. PEDOT:PSS conductivity is successfully increased 3 orders of magnitude. Tailoring PEGDA mechanical properties with addition of high concentration of plasticizers led to hydrogels with compressive moduli ranging between 100 kPa to 100 MPa, still too high to reproduce physiological brain tissue (0.1 to 1 kPa). PEGDA hydrogel transparency was further enhanced by addition of sorbitol.

Keywords: NSC, Scaffolds, Poly(ethylene glycol) diacrylate, Poly(3,4-ethylenedioxythiophene):poly(styrene sulfonate), Electric Field

Neurodegeneration is the progressive loss of structure and function of neurons, characteristic in many neurodegenerative diseases, such as Alzheimer's, Parkinson's, Huntington's or Amyotrophic Lateral Sclerosis¹, affecting an increasing number of people worldwide^{2,3}. To address neurodegeneration, there is a strong research effort to develop tissue engineering strategies that combine stem cell and biomaterial research to address neurodegeneration and neural injury which, allied to a growing market for such therapies for the central nervous system (CNS)^{4,5} and increasing numbers of clinical trials on stem cell-based therapies⁶ place tissue engineering as a very promising pathway for future medical therapies for the CNS. Neural stem cells (NSCs), as the most primordial cells in the CNS, are responsible for the generation of the entire framework of the CNS during pre-natal development, giving rise to several subtypes of neurons and glial cells⁷. NSCs have, as typical of stem cells, two special properties: (i) they are self-renewing, that is, they possess the ability to proliferate, going through numerous cycles of cell division, maintaining an undifferentiated state; (ii) they are multipotent cells, i.e., ability to differentiate into specialized cell types of the CNS, mainly neurons, oligodendrocytes and astrocytes. Besides, NSCs also have unique characteristics, as they present high migratory capacity^{8,9}, having the ability to populate a region during neural development, or repopulate a region that suffered ablation or neurodegeneration; and they can reduce the inflammation and cell death through the release of neurotrophic factors¹⁰⁻¹². However, the limited stem cell number on the adult CNS in specific locations, the formation of glial scar tissue upon injury and the progressive neuronal death associated with neurodegenerative diseases¹³ has the obvious implication that the ability of NSCs to migrate and promote neurogenesis to counteract the onset of these diseases is limited.

The golden standard of tissue regeneration is the use of autologous grafts, where stem cells are isolated from the patient and put under *ex vivo* culture to generate a graft tissue to be implanted in the patient. However, neural autografts

made solely of NSCs have several drawbacks, namely the failure to repair and regenerate the lost neural tissue and the lack of functional integration and recovery of the *ex vivo* neurons when introduced in the tissue¹⁴⁻¹⁷.

In view of this limitation, tissue engineering strategies are being developed linking stem cell culture with biomaterials to create scaffolds, which are structures that attempt to function as an artificial extracellular matrix (ECM), mimicking the physiological microenvironment that control cell growth and differentiation. Scaffolds can be used to enhance NSC *ex vivo* culture and as delivery vehicle for the graft tissue, promoting the integration of functionalization between host and graft^{13,18,19}. To be used for graft development with neural stem cells, a desirable scaffold has to be: biocompatible, causing no cytotoxicity and minimal inflammatory response; the degradability should be controlled to account for tissue integration from the graft into the host; and it has to provide the appropriate biochemical and physical cues to mimic a neuroregenerative microenvironment, promoting NSC adhesion, viability and proliferation, as well as allowing functional integration with the surrounding tissue. Some of these clues include: architecture and three-dimensionality; neurotrophic factors; biochemical cues, such as growth factors and soluble differentiation inducers; surface functionalization with ECM proteins, like laminin or fibronectin, or with their derived peptides; substrate elastic modulus; surface topography and electric cues.

A key characteristic of the functioning CNS is the propagation of electrochemical signals upon action potentials through the neuron, and from neuron to neuron through synaptic transmission. Designing electroconductive scaffolds to electrically stimulate cells should allow a better nerve regeneration on culture and functional integration of the graft by providing the means to elicit action potentials and improve synaptic interconnections^{13,16,20,21}.

There have been some recent reports regarding the effects of electric field on NSCs²²⁻²⁵, all referring an increase in neurite growth, cell elongation and in neural differentiation. Notably,

the recent work by Pires *et al.*²⁵ showed a promising strategy in the use of the conductive polymer poly(3,4-ethylenedioxythiophene):poly(styrene sulfonate) (PEDOT:PSS) to provide such electric cues. However, the mechanisms behind the effect of electric fields on cell culture are still not clear. It is hypothesized that changes in membrane potential and intracellular signal transduction pathways due to the electric field are responsible for the alterations in cell behaviour^{23,25}. Further studies are needed to elicit the mechanisms behind the effect of electric field on expansion and differentiation of NSCs.

This work aims to create transparent, electroconductive scaffolds for NSC culture, serving as platforms to study the influence of electric fields on cell behaviour and to validate the use of the materials and techniques explored in future developments of scaffolds for cell-based therapeutic strategies. Two different pathways were explored: i) printing of 3D printing by fused deposition modelling (FDM) of commercial filaments was used to make customizable, low-cost, easy and quick to produce platforms; ii) a combination of a transparent hydrogel – poly(ethylene glycol) diacrylate (PEGDA) – and the electroconductive conjugated polymer poly(3,4-ethylenedioxythiophene):poly(styrene sulfonate) (PEDOT:PSS) to further establish the use of these biocompatible materials in the development of scaffolds for NSC culture.

The materials of the scaffolds were characterized by electrical conductivity and optical transmittance. Proof-of-concept biological studies of NSC expansion and differentiation were then performed on these scaffolds to assess their viability in the investigation of electrical field effects on cell culture.

PEGDA is a hydrogel with increasing use in biotechnological applications involving cell culture due to its characteristics: PEGDA is biologically inert, as it is non-toxic and does not generate any immunogenic response²⁶; it is transparent, allowing the development of scaffold systems for easy microscopy imaging²⁷; chemical and structural properties can be extensively modified, as well as its mechanical properties, which can be varied over a range of moduli and swelling ratios comparable to many soft tissues^{28,29}. It has been envisaged as a scaffold material for tissues with different stiffness, such as bone³⁰ and cornea³¹, and has been extensively used in cartilage^{32–34}. The usage of PEGDA in neural-related systems is recent: it has been used in the fabrication of neurocompatible hydrogels³⁵ or in the development of injectable drug-delivery systems for the treatment of spinal cord injuries³⁶, such as delivery of nerve growth factor³⁷.

Conductive or conjugated polymers are organic polymers that intrinsically conduct electricity. The backbone of these polymers have contiguous sp²-hybridized carbon centres, each having a valence electron residing in a p_z orbital, orthogonal to the σ-bonds. The π bonds resulting from the combination of these orbitals allow the delocalization of these electrons throughout the polymer backbone^{38,39}. There are several extensively explored conductive polymers, such as polypyrrole, polyaniline and several polythiophene derivatives^{38,40}. One of these polythiophenes – PEDOT:PSS – has gained special relevance over the years. PEDOT:PSS has several advantages over other conductive polymers, such as high transparency in

the visible spectral range, high flexibility, thermal stability and processability in aqueous dispersions^{41,42}, finding several applications in organic electronics, such as organic light-emitting diodes^{43,44}, organic photovoltaic cells^{45,46} and other energy conversion and storage devices, such as supercapacitors^{47,48}, fuel cells⁴⁹ and stretchable devices^{50,51}. Recent medical applications of PEDOT:PSS in the fields of tissue engineering and bioelectronics have emerged due to the biocompatibility⁵² of PEDOT:PSS and its ability to be effortlessly modified in order to promote the immobilization of proteins, creating ideal interfaces with biological systems for organic bioelectronics applications⁵³. For tissue engineering applications, as discussed above, PEDOT:PSS has the ability to provide electrical cues on scaffolds for NSC growth, differentiation and cell orientation^{25,40}.

Materials and Methods

Scaffold Design and Development

A. Production of 3D scaffolds

The scaffold was designed as shown in Figure 1 using SolidWorks 2015 CAD software and extruded by FDM on the MakerBot Replicator 2X using commercial filaments – a transparent filament of poly(ethylene terephthalate) (PET)⁵⁴ and a recently developed electroconductive filament made from poly(L-lactic acid) (PLLA or, more commonly, PLA) mixed with carbon-black (cPLA)⁵⁵.

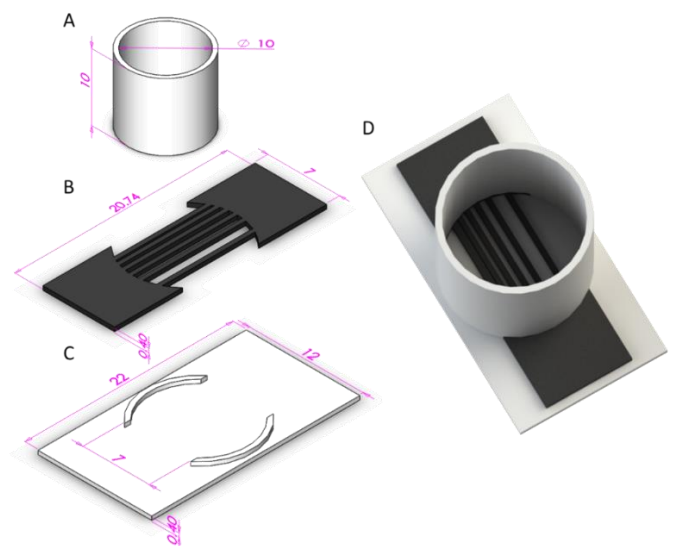


Figure 1. cPLA scaffold design: (A) medium container; (B) cPLA filaments; (C) PET base; (D) Assembled scaffold. Dimensions in mm.

Later, a second iteration was designed, where two cPLA filaments (distanced at 400 μm) ran parallel to each other, forming a conduit with two regions: one where the cPLA is parallel to the orientation of the subjacent PET filaments, the other where it is perpendicular (Figure 2).

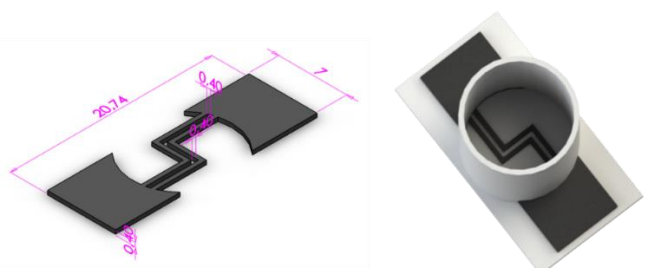


Figure 2. Design of the second iteration of 3DP PET/cPLA scaffold: cPLA filaments (left); assembled scaffold (right). Dimensions in mm.

B. Hydrogel- and Conductive Polymer-based scaffolds

A transparent hydrogel – PEGDA – and an electroconductive conjugated polymer – PEDOT:PSS – are used. PEGDA oligomer solution with a molecular weight of 575 Da (Sigma-Aldrich) was used. First, the 2,2-dimethoxy-2-phenylacetophenone (DMPA, maximum absorption at 365 nm, Sigma-Aldrich) photoinitiator was dissolved (300 mg/ml) in N-vinylpyrrolidone. DMPA solution is then added to the PEGDA at 10 $\mu\text{l/ml}$. To create substrates for ink-jet printing, the solution is filtered with a 0.2 μm syringe filter and is placed in a mold made of two glass slides separated by a 0.8 mm PET spacer created on the extruder, and exposed to UV light (Newport 94023A Sol3A solar simulator, with an intensity of 100 mW/cm^2) for 2 min. The glass slides were previously plasma-treated at 60 W for 6 minutes. The resulting PEGDA substrates are taken from the mold, rinsed with distilled water and dried under a nitrogen stream. A solution of PEDOT:PSS (Clevios P VP Al 4083) with 10 v/v% EG, 0.5 $\mu\text{l/ml}$ TCAA and 10 mg/ml crosslinker GOPS was filtered with 0.45 μm cellulose acetate filter tips and was used to print PEDOT:PSS onto the PEGDA substrates using the Dimatix Materials Printer 2831 (DMP, Fujifilm). A design was created in Inkscape software where PEDOT:PSS stripes of varying widths were designed – in this case, the design had strips with 500, 100, 50 and 20 μm , with gaps of 500 μm (Figure 3).

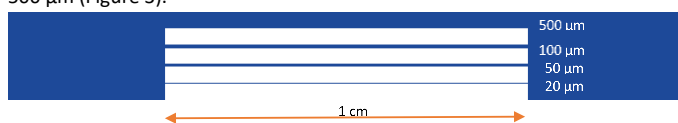


Figure 3. PEDOT:PSS feature used for inkjet-printing on PEGDA.

PEDOT:PSS spin-coated films for electrical conductivity measurements

Glass substrates with an approximate area of 1x1 cm^2 were cut, and sequentially washed with acetone and 2-propanol in an ultrasonic bath for 5 minutes, and rinsed using a nitrogen stream. The glass substrates were then O_2 -plasma treated at 30 W for 6 minutes before use in order to increase their hydrophilicity by creating hydroxyl (-OH) groups on the surface.

1. **PEDOT:PSS (Control).** Simple aqueous PEDOT:PSS dispersion (Clevios P VP Al 4083) was used to spin coat glass substrates at 1800 rpm for 60 seconds, which were thermally annealed at 120 $^{\circ}\text{C}$ for about 10 minutes.

2. **Crosslinked PEDOT:PSS + EG + TCAA**^{25,56,57}. 10 mg/ml crosslinker (3-glycidyloxypropyl)trimethoxysilane (GOPS), 10 v/v% of ethylene glycol (EG) and 0.5 $\mu\text{l/ml}$ trichloroacetic acid (TCAA) were added to PEDOT:PSS dispersion (Clevios P VP Al 4083) and stirred for 24 hours. Glass substrates were then spin coated at 1800 rpm for 60 seconds, thermally annealed at 150 $^{\circ}\text{C}$ for at least 2 minutes to activate the crosslinker and dried under vacuum at 60 $^{\circ}\text{C}$ for 24 hours.

Electrical Conductivity

Electrical conductivity was assessed on PEDOT:PSS films spin-coated on glass using an in-house built 4-point probe setup. Film thickness was measured using a Dektak 3.21 Profiler. Conductivity is given by:

$$\sigma = \frac{l}{R \cdot A} \text{ [S/cm]} \quad (1)$$

where R is the resistance, l the distance between the two electrodes and A is the film cross-sectional area, given by the product of the film thickness by the width.

Cell Culture

A. Cell Line

The cell line used was ReNcell VM human neural progenitor cell line from Millipore, which is derived from the ventral mesencephalon region of human fetal brain and immortalized by retroviral transduction with v-myc oncogene. Cell doubling time is 20-30 hours, and can be differentiated *in vitro* to a high level of human neurons which have been shown to be electrophysiologically active and thus suitable for these experiments.

B. Culture Media

The Basic Culture Medium used in the experiments was prepared using a 1:1 mixture of Dulbecco's Modified Eagle Medium with Nutrient Mixture F12 (DMEM/F12, Life Technologies) supplemented with 1% N-2 (Life Technologies), 20 $\mu\text{g/ml}$ insulin (Life Technologies), 1.6 g/l additional glucose (Sigma) and 1% Penicillin/Streptomycin (Pen/Strep, Gibco®). For expansion, the basic culture medium was further supplemented with 20 ng/ml EGF, 20 ng/ml FGF-2 (both from Peprotech) and 20 $\mu\text{l/ml}$ B27 (Life Technologies). For differentiation, Neurobasal Medium (Life Technologies) was supplemented with B27 (20 $\mu\text{l/ml}$) and mixed in a ratio of 1:1 with basic culture medium.

C. NSC Thawing and Expansion

Prior to their use in the experiments, cells were thawed and cultured for at least one passage. A T12.5 flask is previously coated with laminin: the coating protocol consists on an incubation with 2 ml poly-L-ornithine (Sigma) at the cell incubator (37 $^{\circ}\text{C}$; 5% CO_2) for at least 30 minutes, washed once with PBS and incubated overnight at the cell incubator with 1ml diluted solution of laminin (20 $\mu\text{g/ml}$ in PBS). NSCs were thawed were resuspended in expansion medium (growth factor-supplemented basic culture medium). Cells were thawed at passage 40 from the -80 $^{\circ}\text{C}$ freezer and seeded onto the previously coated T12.5 flask with a density of about 1.5×10^5 cells/ cm^2 and expanded until reaching 80-90% confluence.

Electric Field Experiment

A. Scaffold Preparation and NSC Seeding

To prevent culture medium leakage, a watertight enclosure made of polydimethylsiloxane (PDMS) was created around both scaffolds. Copper wires of 0.35 mm diameter were used to make the connection between the scaffold electrodes inside the well-plate and the electrodes placed on the cell incubator by gluing one of the wire tips to each of the scaffold electrodes using conductive silver paste (Electrodag 1415, Agar Scientific). Scaffolds are brought to a sterile environment on the laminar-flow chamber, glued to 6-well plates using Medical Adhesive Glue (Dow Corning) and sterilized using Gibco® Antibiotic-Antimitotic solution for at least 2 hours. The scaffolds are coated with laminin with the same procedure used for the T-flask. Previously expanded NSCs are seeded onto scaffolds with a density of 30 000 cells/ cm^2 using the expansion culture medium.

B. NSC Expansion

An AC electric field was applied as a voltage quadratic pulse of 100 Hz during 4 consecutive days after seeding; the expansion culture medium was changed every 2 days.

Expanded cells were first washed twice with PBS and fixed with 4% paraformaldehyde (PFA) at room temperature for 30 minutes. They were then washed twice with PBS and permeabilized with blocking solution (89.9% PBS; 10% Normal Goat Serum (NGS) and 0.1% Triton-X) for 30 minutes. The samples were then washed twice with PBS, incubated with 1:1000 dilution of phalloidin-tetramethylrhodamine B isothiocyanate (Phalloidin-TRITC, 1 $\mu\text{l/ml}$ in PBS) for 45 minutes in the dark, washed again twice and incubated with 4',6-diamidino-2-phenylindole (DAPI, 1.5 $\mu\text{l/ml}$ in PBS) for 5 min in the dark. The samples were finally washed twice and stored with PBS for microscopic imaging.

After fluorescence staining and microscopy, samples were dehydrated by sequentially immersing in 25%; 50%; 75% and 99% ethanol in milliQ water, at 37 $^{\circ}\text{C}$ for 30 minutes each. The dehydrated samples were then coated with Au/Pd layer of about 30 nm using a Polaron E5100 coater (Quorum Technologies). All images were obtained using an electron beam with energies in the range of 10-15 keV, with a Field Emission Gun Scanning Electron Microscope (FEG-SEM, JEOL JSM-7001F) at magnitudes of 100x and 400x. At least 3 images were taken for each magnitude and for each of the spaces between cPLA filaments or PEDOT stripes, depending on the type of scaffold in use.

NSC Morphology and Alignment Analysis

For the 4-days expansion experiments, cell morphology was analysed according to aspect ratio (ratio between longest and shortest axis of cell body), while cell alignment was analysed by creating histograms of the angle between the longest cell axis and the direction of the electric field; angle histograms are represented as the frequency percentage, and range from -90 $^{\circ}$ to 90 $^{\circ}$. The analysis was performed with FIJI software in both cases; at least 15 cells were analysed in a minimum of 3 images for each of the spaces between cPLA filaments, in the case of the PET/cPLA scaffolds, or on top of the PEDOT stripes, for the PEGDA/PEDOT scaffolds.

C. NSC Differentiation

Cells are expanded by applying an AC electric field as a voltage quadratic pulse of 100 Hz during 4 consecutive days after seeding, with the expansion medium being changed every 2 days; after 4 days, differentiation is induced by changing the medium into the differentiation one (with Neurobasal Medium and lack of EGF and FGF-2 growth factors) and replaced every 3 days, while the AC electric field is applied during 7 days intermittently with a daily 4-6h rest period. In some trials, live cell Calcein AM staining was performed at day 4.

After 7 days, immunocytochemistry was performed on the differentiation experiments in order to compare differentiation levels on scaffolds of early neurons (marked with β -Tubulin III – TuJ1, red) and astrocytes (marked with Glial Fibrillary Acidic Protein – GFAP, green) under electric stimulus and

control. Cells were first washed twice with PBS and fixed with 4% PFA at room temperature (RT) for 30 minutes. The samples were then washed twice with PBS and permeabilized with blocking solution for 30 minutes. The primary antibodies were then diluted in a staining solution (94.9% PBS; 5% NGS and 0.1% Triton-X) and used to incubate the samples at 4°C overnight in the dark (1:4000 in Mouse IgG Anti-Tuj1 and 1:150 in Rabbit IgG Anti-GFAP). The samples were then washed once with PBS and incubated with the secondary antibodies (Alexa Fluor- 546/Goat Anti-Mouse IgG and Alexa Fluor-488/Goat Anti-Rabbit IgG) at RT for 1 hour in a dark cabinet, both with 1:500 dilution in staining solution. Finally, samples were rinsed once with PBS, incubated with DAPI at RT for 2 minutes in the dark, and washed twice and stored with PBS for fluorescence microscopy.

Results and Discussion

Scaffold Design and Development

A. Production of 3D Scaffolds

Scaffold design and printed result are shown in Figure 4.A and B, respectively. Macroscopically, the result is very similar to the design. However, when scaffolds were observed under a stereomicroscope, it was possible to observe that the gap separation between cPLA filaments in the extruded scaffolds was different from the ones projected on the design. Additionally, when several scaffolds were extruded, it was observed that the gap size between cPLA filaments was not constant through scaffolds. These design-scaffold disparities, namely smaller-than-design gaps and the fact that shrinkage is not observed on the same proportion in filament width is probably because extra polymer is being extruded by the nozzle. This could be due to inadequate printing settings, namely the speed at which the plastic is extruded could be too high, or could be due to the precision of the machine used, as these details are the same size or smaller than the nozzle diameter. Also, this could be due to the diameter of the commercial filament. The printer filaments usually have a tolerance associated to its diameter – for cPLA, it is 3%, which means that filament diameter is $1.75 \pm 0.0525 \text{ mm}^{55}$. When extruding the filament, this error will approximately duplicate that of the extruded filament⁵⁸, which may contribute to increase the width and thus counteract thermal contraction.

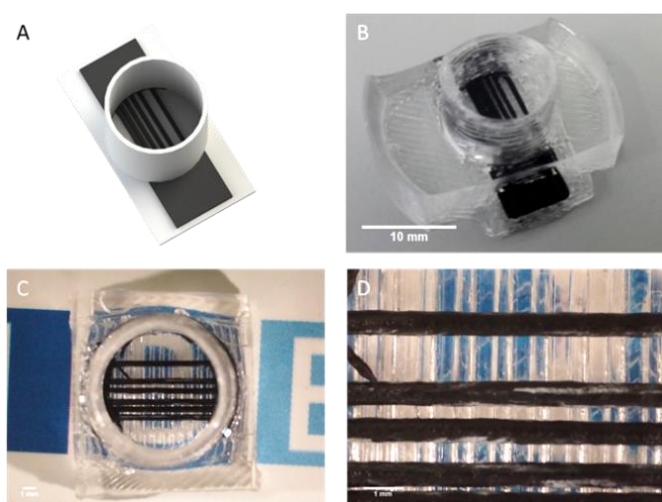


Figure 4. 3D-printed PET/cPLA scaffold: (A) Design in SolidWorks; (B) printed result (scale bar at 10 mm); (C) and (D) show PET transparency and the gap separation between cPLA filaments in detail, respectively (scale bars at 1 mm).

Overall, these differences in detail size show that the machine used is not appropriate to print features with dimensions below 1 mm for applications needing accurate feature size, as

this becomes similar to the dimensions of the variations caused by thermal expansion/contraction and extruding errors. Higher-resolution machines that can print smaller features and work with biocompatible materials exist and should be used for applications similar to those addressed in this work.

In terms of transparency, the underlying PET base is relatively transparent as shown in Figure 5. However one can observe the “wavy” surface that is a result of the printing process itself, as several cylindrical filaments are extruded during printing and fused together during cooling. This PET surface pattern limits cell visualization, as it is only possible to focus on cells at the same height. As shown in Figure 5.A, this window of visualization is only around 50 μm , while the filament has a diameter of 400 μm . This window of visualization is probably situated on top of the filament as represented in Figure 5.C, where the material surface is almost flat, which leads to minimal deflection of light rays and number of internal reflections, thus higher transmittance. Also, when cells were seeded on scaffolds, it was possible to see that it was not even possible to focus on cells in some areas, most likely due to the scattering of light on the material. This scattering can be caused by internal reflections on the cylindrical threads, which result in these “dark” spots where it is impossible to focus.

Furthermore, irregularities on the extruded filament, both at the surface or inside the filament, can lead to scattering – in fact, as can be observed in images taken on the SEM (Figure 5.B), the PET substrate presented some concave indents on the surface that could interfere with the trajectory of the light rays. The scattering of light severely impaired the quality of the fluorescence microscopy images taken, as it lead to an increase in intensity on the background light which limits the visualization of the cell structures marked by the probes, especially in red and green-fluorescent images. Also, with these scaffolds, care should be taken on analysing morphological changes or cell alignment, as these could be a result of the topography created on the cell culture supporting surface with this wavy PET pattern.

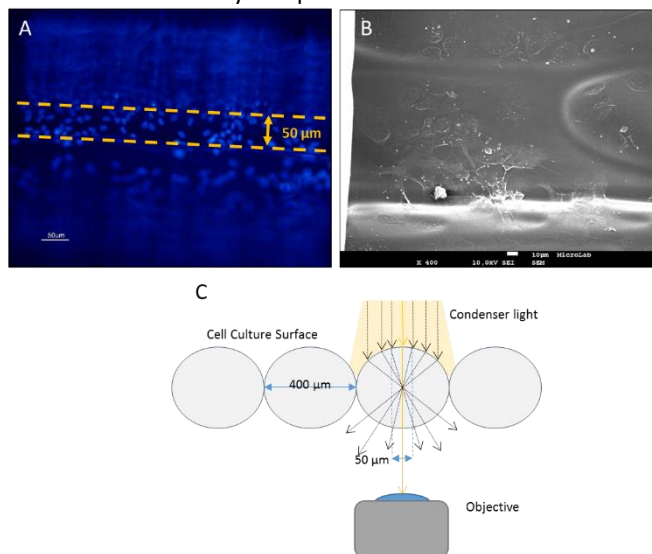


Figure 5. Cell Visualization on PET filaments: (A) FM image of cell nuclei stained with DAPI (scale bar at 50 μm) – it is possible to see a window of about 50 μm width where cells are in focus; (B) SEM image, showing cells and the topography of PET filaments (right, scale bar at 10 μm); (C) the window of visualization corresponds to the region where there are less internal reflections of light rays, thus it is possible to focus on the transmitted light in the inverted optical microscope and observe cells.

To obtain better images, confocal microscopy should be performed on these substrates in order to eliminate the scattered light, as it eliminates out-of-focus light, and permits to reconstruct a 3D visualization of the several planes created by the PET pattern. Furthermore, a simpler system, where cPLA filaments are extruded onto a clear, smooth substrate (as in a well-plate or a Petri dish) could be used to conduct the NSC experiments described in this work to validate the use of cPLA as a means to convey an electrical field to cells and study its effect, obtaining clear images while reducing any topography effect.

The resistivity/conductivity of cPLA was determined before extrusion, in a piece of filament, and after extrusion in a cylindrical sample. The resistivity values obtained, 17.24 and 29.95 $\Omega\cdot\text{cm}$, are very similar to the ones obtained by the manufacturer⁵⁵ – 15 and 30 $\Omega\cdot\text{cm}$ before and after extrusion, respectively.

The drop of conductivity upon extrusion is likely due to a rearrangement of the conductive carbon-black aggregates present in PLA. Upon heating in the nozzle and quick cooling at the platform, it is possible that aggregates of smaller dimensions are formed when compared to the ones obtained during the fabrication of the commercial filaments. In fact, spherulite growth rate in PLA/carbon black blends is very low at the temperature used for solidification of the extruded filaments (70°C)⁵⁹. These hypothesized smaller aggregates will lead to the increase in particle boundaries in a given volume, increasing the energy barrier for charge transportation between aggregates, thus decreasing conductivity. The reduction of aggregate size after extrusion requires evidence, which can be obtained upon AFM analysis of topographic and phase images of planar cPLA substrates with AFM.

The conductivity value of 0.03 S/cm obtained after extrusion is adequate for the intended purpose, as it is 300 times superior to the established minimum value (10^{-4} S/cm). However, the scaffolds showed resistance values on the order of 1 k Ω , possibly due to the high impedance between the silver paint and the cPLA. This value is still acceptable, as one can deliver a current as high as 1000 μA given the voltage limit of 1 V/cm.

B. Hydrogel- and Conductive Polymer-based scaffolds

Figure 6.C, D and E evidence the IJP process as drops can be discriminated. Printed features measured on scaffold images showed different sizes than the designed specifications – for example, one scaffold resulted in bands with widths of 450, 143, 74 and 36 μm , when compared to the design sizes of, respectively, 500, 100, 50 and 10 μm . These differences are due to the ink drop size, which ultimately affects printing resolution and the size of the printed features. In view of the average size of drops shown in Figure 6.F, which sets the size of the smallest feature (around 30 μm), the band widths are approximately multiples of this value, as the bands are printed as several parallel lines of ink. Nevertheless, opposite to what happened in FDM, the results are more reproducible in IJP, as several printed PEDOT:PSS designs had essentially the same feature sizes. Therefore, to print features of the same sizes as in the design, the ink drop size should be reduced.

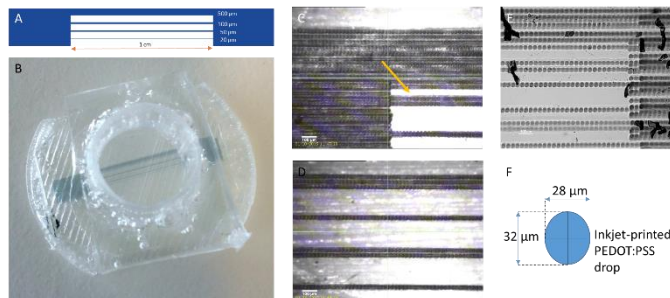


Figure 6. PEGDA/PEDOT:PSS scaffold: (A) Design of the IJP PEDOT:PSS film; (B) Scaffold with printed PEDOT:PSS (blue) on top of transparent PEGDA – a 3DP medium container was glued on top and covered around with PDMS to enclose the medium and separate the internal cell culture area from the external PEDOT:PSS electrodes (scale bar at 10 mm); (C) and (D) show IJP features taken with the inbuilt DMP camera – the yellow arrow on C shows a region lacking PEDOT:PSS due to nozzle failure during printing (scale bar at 100 μm); (E) IJP feature taken with the optical microscope, where it is possible to distinguish printed drops (scale bar at 100 μm); (F) Average size of the inkjet-printed PEDOT:PSS drops.

The size of ink drops on the substrate, and thus printing resolution and minimum feature size, is dependent on several factors, such as: fluid viscosity; the speed at which the ink material dries; surface interaction between the ink material and the substrate material; and voltage function used in the piezoelectric nozzle to mold the shape of the ink drop. In IJP applications, it is always much simpler to modify the variables at the substrate level, such as modifying surface groups at the substrate for higher or lower affinity to ink, influencing ink spreading, or speeding up the drying of the ink with platform heating, than modifying parameters that affect the shape of the drop deposited, such as viscosity and piezoelectric voltage function. One could also create, by lithographic techniques such as soft lithography, a PEGDA substrate with “valley” features with a desired size to confine PEDOT:PSS ink and prevent its spreading.

When looking at the edges of the printed feature, we observe the superposition of different layers of ink (Figure 6.C, D and E). It is important to note that film thickness is not completely additive, i.e., it is not the direct sum of the thickness values of each layer because the new layer is not printed directly above the previous ones. This presents a problem for the estimation of how many layers should be printed in order to obtain films with a desired thickness.

It is common to identify printing “gaps”, that is, absence of ink deposition, like the one indicated by the yellow arrow in Figure 6.C. This is due to nozzle malfunctioning. The most probable reason is the drying of PEDOT:PSS inside the nozzle, or accumulation of micro aggregates present in the solution, which clog the nozzle. This phenomenon justifies the need to filter the solution before injecting it in the cartridge. Also, its frequency is diminished thanks to the cleaning cycles, which will pause the printing, move the cartridge to a blotter, and “purge” the cartridge, that is, force the liquid to come out of the nozzles, which clears up the accumulated debris in most cases. Nonetheless, this common occurrence is a severe problem when huge importance is given to feature size.

As shown in Figure 7, the pure PEGDA substrate is almost transparent, as it is possible to focus on cells and the PEDOT:PSS ink dots.

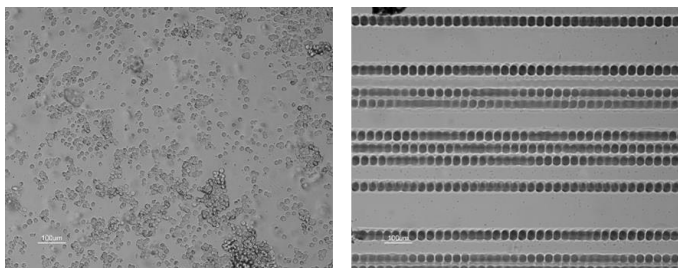


Figure 7. PEGDA substrate showing good cell (left) and inkjet-printed PEDOT:PSS (right) visualization by the optical microscope (Scale bars at 100 μm).

The UV-crosslinked PEGDA presents very good transparency, appropriate to both optical and fluorescence microscopy. However, the material is very stiff and brittle, which makes it difficult to handle, and inappropriate to be used for development of grafts for the CNS, as it will not recreate the physiological mechanical properties of the surrounding tissue. This dictates the need to explore methods to change the mechanical properties of PEGDA.

The conductivity of PEDOT:PSS used for IJP (0.8 S/cm, which is higher than that of the as-received PEDOT:PSS, 9.1×10^{-4} S/cm) is fit for this application. The conductivity values of cPLA are lower than those obtained with the modified solution of PEDOT:PSS, which is understandable given that cPLA is a blend of non-conductive PLA and carbon-based materials, such as graphene. This would lead to the wrong assumption that PET/cPLA scaffolds were less conductive than the PEGDA/PEDOT:PSS ones; however, in practice the first scaffold is created with extruded cPLA filaments, while the last will have only a thin inkjet-printed PEDOT layer with a thickness in the range of 10-100 μm . Therefore, for the same length of material, the cPLA will have a larger section area, and thus smaller resistance when compared to the PEDOT:PSS film. This is proven by the typical resistance values obtained with scaffolds: the cPLA ones have values on the order of 1 k Ω , while the PEDOT:PSS ones are around 1 M Ω , both measured at a distance of 1 cm.

Similarly to the cPLA, the impedance between the silver paste contact and the PEDOT:PSS film can lead to an increase of the resistance of the scaffold. In both cases, this could be improved by coating the cPLA or PEDOT:PSS electrodes, that is, outside the area of cell culture, with a thin layer of thermal evaporated gold, as made in the procedure of the conductivity determination. Although not assessed in this work, there is an obvious need to further study the influence of the modifiers added to PEDOT:PSS on cell viability and attachment to the created films, especially concerning the use of TCAA. The processing steps of PEDOT:PSS can have a huge impact on the toxicity of the resulting films. However, placing the modified PEDOT:PSS films under vacuum with heating can reduce their toxic agents content.

Since substrates made of pure UV-crosslinked PEGDA did not show significant change in volume during swelling, the integrity of PEDOT:PSS was not compromised, maintaining its electrical resistance. In order to establish the viability of using PEDOT-coated PEGDA hydrogels, especially on more flexible, viscoelastic PEGDA hydrogels, methods should be explored to increase the flexibility of PEDOT:PSS films. One of the strategies that could be employed to solve this problem is the

addition of plasticizers to PEDOT:PSS, similarly to the modifications made on the mechanical properties of PEGDA in this work, as described below. These modifications should be assessed by measuring the mechanical properties of PEDOT:PSS, especially ductility and resistance variation of PEDOT:PSS films with bending by performing inner and outer bending reliability tests, as well as fatigue tests^{60,61}.

Electric Field Effect on NSC Culture

A. Effect of Electric Field on Morphological Changes and Cell Alignment during NSC Expansion.

During the NSC differentiation protocol on these scaffolds, live imaging of cells was performed after 4 days of expansion by staining with Calcein AM. In Figure 8, it is possible to observe FM images of the cells lying on the three bands under electric field and for the control, as well as the angle histograms for each condition. These are a superposition of bright field images with fluorescent ones.

For horizontal gaps, there is a Gaussian curve centred at angles near 0° when the electric field was applied, while in the control there was no preferential orientation, as the histogram showed a uniform distribution. This suggests that the orientation is induced by the electric field, but care has to be taken when establishing such a conclusion, as this is also the orientation of the topography of the PET substrate. There is the need to separate the topographical cues from the electrical ones in cell alignment in future studies.

For vertical gaps, there is a strong evidence for the influence of the electric field on cell orientation, as its application resulted in cell alignment parallel to the electric field, when compared to control, where cells had a tendency to align according to the orientation of the PET substrate topography, that is, perpendicular to the direction of the electric field. However, there is a lack of statistical significance on the histogram for the electric field condition, as a reduced number of cells was observed and their orientation established.

Regarding aspect ratio (Figure 9), it increases for cells on the vertical gaps when electric field is applied, thus we may conclude that elongation is influenced by the electric field. For the horizontal gaps, however, both cells under electric field and on control had statistically the same aspect ratio, which is the same for the control condition in the vertical gaps. It is possible that there is a lower effect of the electric field on cells in the horizontal gaps which were much wider (about 500 μm wide) than the vertical ones (about 200 μm wide). This may indicate that the orientation of cells parallel to the direction of the applied electric field on horizontal gaps may be, in fact, the result of the topography of the PET substrate rather than the result of the electric field.

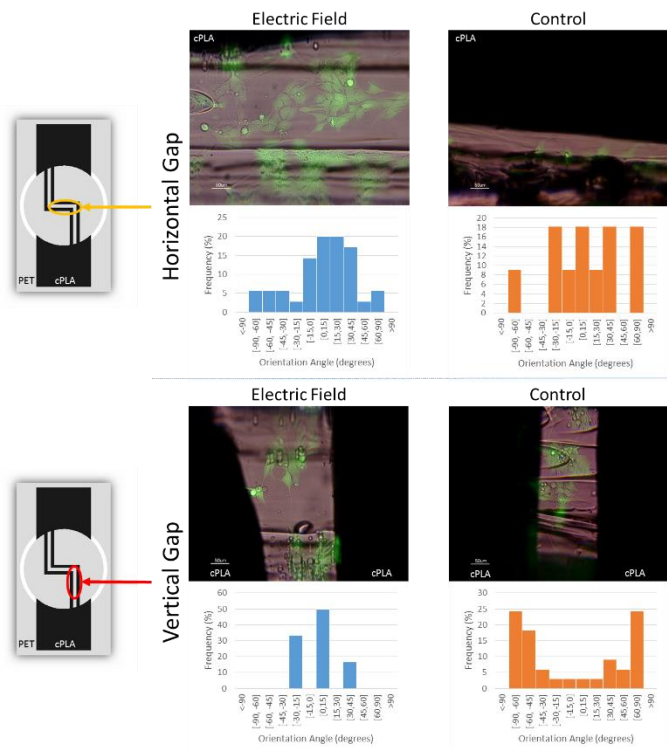


Figure 8. Overlay of bright-field and FM images of Calcein AM-stained cells (scale bars at $50\ \mu\text{m}$) and electric field vs. control angle histograms on cPLA filament gaps.

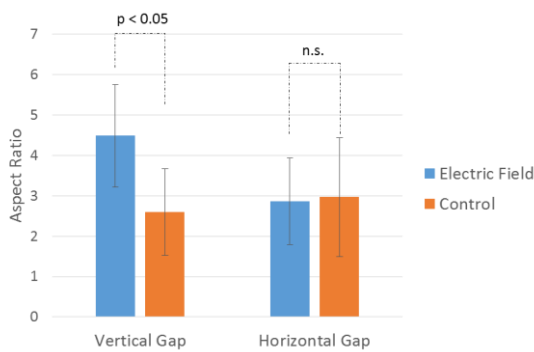


Figure 9. Electric field vs. control aspect ratio for NSCs on vertical and horizontal gaps in scaffolds of PET/cPLA with curves.

There is the need to study the effective electric field that act on cells; even if the voltage applied was lower than the one that causes electrolysis of water, there is probably an effect on the culture medium, which is basically an electrolyte. When subjected to an electric field, this induces ionic currents in the medium that can, for example, alter the pH and influence cell viability. Also, there is the need to study the electric field generated in the scaffold. Theoretically, the electric field generated runs parallel to the two cPLA filaments, but minor differences in resistance between the filaments leads to different currents passing through them for the same applied voltage potential, thus creating a small electric field perpendicular to the filaments, which can also have an influence on cells.

As discussed, it was not possible to observe cells using optical microscopy nor fluorescence in the PEGDA/PEDOT:PSS scaffolds due to the bending of the substrate. However, SEM images had good quality, so they were used to assess NSC morphology and cell alignment. The results are discriminated by PEDOT:PSS printed band size, and measurements were

made for both conditions (electric field and control) on cells situated on three of the four bands: $500\ \mu\text{m}$ (wide band), $100\ \mu\text{m}$ (medium band) and $50\ \mu\text{m}$ (narrow band). The actual sizes of the bands are different as explained above, but for simplification purposes they are referenced with the design sizes. Figure 10 shows SEM images of the three bands for electric field and control samples, as well as the angle histograms for each condition.

It was expected that under electric field cells would be oriented along the electric field for the three bands, that is, it was expected that angles near 0° would be more frequent, with the histogram following a Gaussian curve centred at 0° . For control, it was expected that orientation was random, with the histograms representing a uniform distribution across the angle range. This is relatively evident on the histograms for electric field and control conditions on the wide and medium bands.

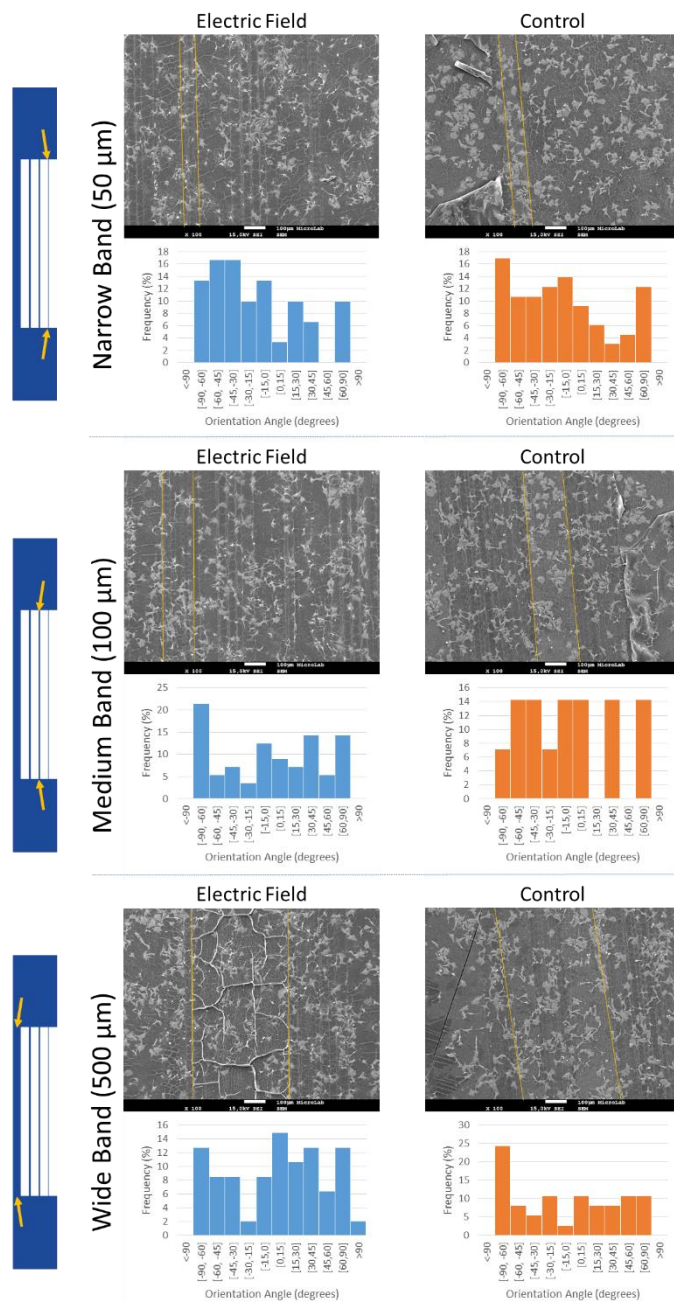


Figure 10. SEM Images (scale bars at $100\ \mu\text{m}$) and electric field vs. control angle histograms on PEDOT:PSS bands.

Regarding NSC morphology, it is evident that aspect ratio (Figure 11) is increased, that is, cells are more elongated when an electric field is applied, in agreement with previous reports^{22,25}. Additionally, there seems to be a slight increase in aspect ratio as the band width is increased – this may be due to an increased effect of the electric field on NSCs for wider bands, as the resistance will be lower due to the higher cross section, thus the current that passes them will be higher. As expected, aspect ratio for control situations is practically the same, except for the wide band. This could be due once again to the topographical cues on the wider PEDOT:PSS band. Further studies are needed to assess the electric field induced cell alignment. Future work on these scaffolds should focus on diminishing the topographic effects on elongation and alignment, in order to have a platform where the influence of the applied the electric field on these parameters could be assessed in a more precise way.

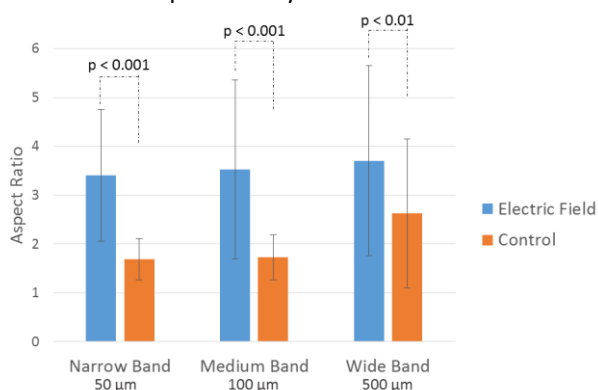


Figure 11. Effect of the electric field on the aspect ratio of NSCs on PEDOT:PSS.

B. Effect of Electric Field on the Commitment to Neuronal or Astrocyte Differentiation Pathways.

It is possible to observe on Figure 12 the results after NSC differentiation on the PET/cPLA scaffold with curves. In a first analysis, it seems that the signal for Glial Fibrillary Acidic Protein (GFAP) is stronger than for TuJ1, which is in agreement with previous studies, given that the NSCs committed to a neuronal lineage are less common than those committed to astrocytes. However, after a more careful analysis it is possible to conclude that there is a majority of cells stained both with GFAP and TuJ1. This eliminates any possible attempt to further analyse the effect of electric field on the differentiation of NSCs by analysing the relative populations of TuJ1-positive cells (early and mature neurons) or GFAP-positive cells (early and mature astrocytes).

It is difficult to assess with the available information what led to failure of the immunocytochemistry experiments. There is a remote possibility that cells are in fact expressing both markers. A population of GFAP-positive cells also expressing the marker for β -III Tubulin TuJ1 has been found in samples of human fetal (18 to 20 weeks of gestation) brain tissue⁶². It may be that the fetal NSC line used in these experiments are, after differentiation, giving origin to these GFAP-positive cells that also express β -III Tubulin, but this is not in agreement with similar experimental conditions in previous studies with the ReNcell VM NSC line^{25,63}.

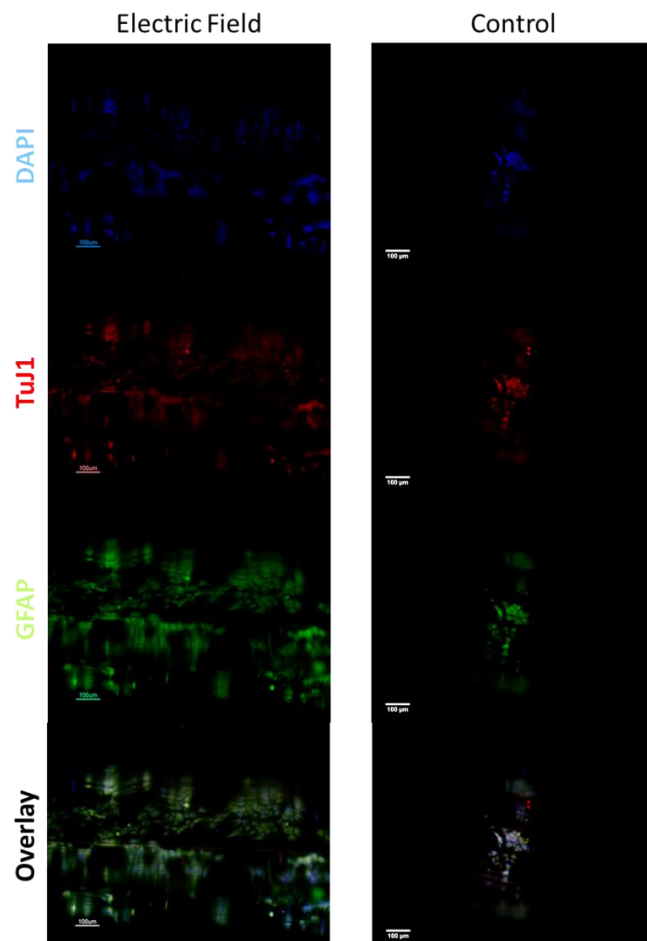


Figure 12. FM Images of DAPI, TuJ1 and GFAP staining, and their overlay after differentiation on the PET/cPLA scaffolds with curves, with and without electric field (scale bars at 100 μm). It is possible to note the overlay between TuJ1 and GFAP signal by the yellowish colour on the bottom images.

Besides this problem with immunocytochemistry, a large part of cells on the scaffold were death after differentiation – curiously, most of the death cells were outside the cPLA filaments, so in principle less exposed to the electric field. Again it is possible that electrolyte currents in the culture medium are being induced, which may be affecting these cells outside the filaments. Troubleshooting would involve optimizing culture conditions without electric field to understand when is viable to start inducing differentiation, and assess cell viability with and without electric field conditions. Additionally, appropriate controls for primary and secondary antibodies used in immunocytochemistry to mark GFAP and TuJ1 should be performed.

Conclusions and Future Trends

The main goal of this work was the establishment of scaffold platforms to study the effect of electric field on NSC culture. The proposed platforms were developed and able to be used in proof-of-concept electric field effect studies, but several optimization steps are needed.

On the PET/cPLA scaffolds, the high conductivity provided by the cPLA filaments allows the application of a wide range of current values, but the transparency of the PET substrate is very limited due to its geometry, as cells could only be focused at specific areas– it could be addressed in the future if confocal microscopy would improve the overall visualization of cells.

Besides limited visualization, the characteristic surface topography may influence the orientation of cells, as assessed after expansion of NSCs; immediate future iterations of this scaffold could be tested using a simpler transparent substrate, such as glass or polystyrene substrate with the extruded cPLA filaments on top.

This scaffold was an attempt to present a commercial additive manufacturing system as viable tool for the construction of customized platforms or scaffolds for cell culture. The limitation in printing 3D motifs with sizes on the order of 100 µm, related to cPLA gap size, severely impairs the viability of using this machine for this specific application. Nevertheless, there are systems being developed that allow to print features much smaller with higher resolution, namely FDM bioprinters with 10 µm resolution, with emerging use in the design and production of vascular grafts^{64,65}, or bioprinters using hydrogel and inkjet technology⁶⁶.

With the aim to explore the use of these materials for NSC culture and to study the effect of electric field on these cells, this work succeeded in further establishing PEGDA and PEDOT:PSS as biomaterials for the development of Tissue Engineering strategies, especially hinting its use for the CNS: both PEGDA transparency and electroconductivity and resolution of IJP PEDOT:PSS were satisfactory. In the immediate future, further expansion and differentiation studies with electric fields on this platform should be done.

Regarding proof-of-concept electric field effect on NSC studies performed, further work is needed in order to: i) validate the developed platform for these studies; ii) understand, characterize and compare the effects of different electric field conditions on NSCs, such as current/voltage intensity, pulse duration and period of stimulation, as well as to elicit the mechanisms behind the effect of electric field on expansion and differentiation of NSCs; iii) perform a physical and chemical characterization, biocompatibility and influence on cell culture of the materials explored in this work.

References

1. Bredesen, D. E., Rao, R. V. & Mehlen, P. Cell death in the nervous system. *Nature* **443**, 796–802 (2006).
2. Prince, M. et al. *World Alzheimer Report 2015 - Alzheimer's Disease International*. (2015).
3. Dickson, D. W. Parkinson's disease and parkinsonism: neuropathology. *Cold Spring Harb. Perspect. Med.* **2**, (2012).
4. Shields, D. Regenerative Medicines Market (Technology, Application and Geography) - Size, Global Trends, Company Profiles, Demand, Insights, Analysis, Research, Report, Opportunities, Segmentation and Forecast, 2013 - 2020. (2014). at <<https://www.alliedmarketresearch.com/regenerative-medicines-market>> (accessed November 18, 2015).
5. Lee, S., Kwon, T., Chung, E. K. & Lee, J. W. The market trend analysis and prospects of scaffolds for stem cells. *Biomater. Res.* **18**, 11 (2014).
6. Trounson, A. & McDonald, C. Stem Cell Therapies in Clinical Trials: Progress and Challenges. *Cell Stem Cell* **17**, 11–22 (2015).
7. Kim, S. U. & de Vellis, J. Stem cell-based cell therapy in neurological diseases: a review. *J. Neurosci. Res.* **87**, 2183–200 (2009).
8. Benedetti, S. et al. Gene therapy of experimental brain tumors using neural progenitor cells. *Nat. Med.* **6**, 447–50 (2000).
9. Müller, F.-J., Snyder, E. Y. & Loring, J. F. Gene therapy: can neural stem cells deliver? *Nat. Rev. Neurosci.* **7**, 75–84 (2006).
10. Gage, F. H. Mammalian Neural Stem Cells. *Science (80-)*. **287**, 1433–1438 (2000).
11. Lu, P., Jones, L., Snyder, E. & Tuszynski, M. Neural stem cells constitutively secrete neurotrophic factors and promote extensive host axonal growth after spinal cord injury. *Exp. Neurol.* **181**, 115–129 (2003).
12. Adami, R., Scesa, G. & Bottai, D. Stem cell transplantation in neurological diseases: improving effectiveness in animal models. *Front. Cell Dev. Biol.* **2**, 17 (2014).
13. Mammadov, B., Sever, M., Guler, M. O. & Tekinay, A. B. Neural differentiation

- on synthetic scaffold materials. *Biomater. Sci.* **1**, 1119 (2013).
14. Yu, X. & Bellamkonda, R. V. Tissue-engineered scaffolds are effective alternatives to autografts for bridging peripheral nerve gaps. *Tissue Eng.* **9**, 421–30 (2003).
15. Mahoney, M. J. & Anseth, K. S. Three-dimensional growth and function of neural tissue in degradable polyethylene glycol hydrogels. *Biomaterials* **27**, 2265–74 (2006).
16. Subramanian, A., Krishnan, U. M. & Sethuraman, S. Development of biomaterial scaffold for nerve tissue engineering: Biomaterial mediated neural regeneration. *J. Biomed. Sci.* **16**, 108 (2009).
17. Bottai, D., Madaschi, L., Di Giulio, A. M. & Gorio, A. Viability-dependent promoting action of adult neural precursors in spinal cord injury. *Mol. Med.* **14**, 634–44 (2008).
18. Yang, S., Leong, K., Du, Z. & Chua, C. The design of scaffolds for use in tissue engineering. Part I. Traditional factors. *Tissue Eng.* **7**, 679–89 (2001).
19. Struzyna, L., Harris, J. & Katiyar, K. Restoring nervous system structure and function using tissue engineered living scaffolds. *Neural Regen. Res.* **10**, 679–85 (2015).
20. Siskin, B. F., Kanje, M., Lundborg, G., Herbst, E. & Kurtz, W. Stimulation of rat sciatic nerve regeneration with pulsed electromagnetic fields. *Brain Res.* **485**, 309–16 (1989).
21. Shi, G., Rouabhia, M., Meng, S. & Zhang, Z. Electrical stimulation enhances viability of human cutaneous fibroblasts on conductive biodegradable substrates. *J. Biomed. Mater. Res. A* **84**, 1026–37 (2008).
22. Chang, K.-A. et al. Biphasic electrical currents stimulation promotes both proliferation and differentiation of fetal neural stem cells. *PLoS One* **6**, e18738 (2011).
23. Ghasemi-Mobarakeh, L. et al. Application of conductive polymers, scaffolds and electrical stimulation for nerve tissue engineering. *J. Tissue Eng. Regen. Med.* **5**, e17–35 (2011).
24. Kam, N. W. S., Jan, E. & Kotov, N. A. Electrical stimulation of neural stem cells mediated by humanized carbon nanotube composite made with extracellular matrix protein. *Nano Lett.* **9**, 273–8 (2009).
25. Pires, F., Ferreira, Q., Rodrigues, C. A. V., Morgado, J. & Ferreira, F. C. Neural stem cell differentiation by electrical stimulation using a cross-linked PEDOT substrate: Expanding the use of biocompatible conjugated conductive polymers for neural tissue engineering. *Biochim. Biophys. Acta - Gen. Subj.* **1850**, 1158–68 (2015).
26. Lynn, A. D., Kyriakides, T. R. & Bryant, S. J. Characterization of the in vitro macrophage response and in vivo host response to poly(ethylene glycol)-based hydrogels. *J. Biomed. Mater. Res. A* **93**, 941–53 (2010).
27. Chung, K. et al. Structural and molecular interrogation of intact biological systems. *Nature* **497**, 332–7 (2013).
28. Buxton, A. N. et al. Design and characterization of poly(ethylene glycol) photopolymerizable semi-interpenetrating networks for chondrogenesis of human mesenchymal stem cells. *Tissue Eng.* **13**, 2549–60 (2007).
29. Castro, D. et al. Characterization of solid UV cross-linked PEGDA for biological applications. in *2013 IEEE 26th Int. Conf. Micro Electro Mech. Syst.* 457–460 (IEEE, 2013). doi:10.1109/MEMSYS.2013.6474277
30. Yang, F. et al. The effect of incorporating RGD adhesive peptide in polyethylene glycol diacrylate hydrogel on osteogenesis of bone marrow stromal cells. *Biomaterials* **26**, 5991–8 (2005).
31. Kadakia, A. et al. Hybrid superporous scaffolds: an application for cornea tissue engineering. *Crit. Rev. Biomed. Eng.* **36**, 441–71 (2008).
32. Bryant, S. J. & Anseth, K. S. Hydrogel properties influence ECM production by chondrocytes photoencapsulated in poly(ethylene glycol) hydrogels. *J. Biomed. Mater. Res.* **59**, 63–72 (2002).
33. Gabler, S., Stampfl, J. & Koch, T. Determination of the viscoelastic properties of hydrogels based on polyethylene glycol diacrylate (PEG-DA) and human articular cartilage. *Int. J. Mater. Eng. Innov.* **1**, 3–20 (2009).
34. Roberts, J. J. & Bryant, S. J. Comparison of photopolymerizable thiol-ene PEG and acrylate-based PEG hydrogels for cartilage development. *Biomaterials* **34**, 9969–9979 (2013).
35. Li, X., Liu, X., Zhang, N. & Wen, X. Engineering in situ cross-linkable and neurocompatible hydrogels. *J. Neurotrauma* **31**, 1431–8 (2014).
36. O'shea, T. M. Injectable hydrogels for the improved delivery of treatments in spinal cord injury. (2014). PhD Thesis. Massachusetts Institute of Technology.
37. Stukel, J., Thompson, S., Simon, L. & Willits, R. Polyethylene glycol microgels to deliver bioactive nerve growth factor. *J. Biomed. Mater. Res. A* **103**, 604–13 (2015).
38. Kiess, H. G. *Conjugated Conducting Polymers*. **102**, (Springer Berlin Heidelberg, 1992).
39. Harun, M., Saion, E. & Kassim, A. Conjugated conducting polymers: A brief overview. *J. J. Adv. Sci. Arts* **2**, 63–68 (2007).
40. Balint, R., Cassidy, N. & Cartmell, S. Conductive polymers: towards a smart biomaterial for tissue engineering. *Acta Biomater.* **10**, 2341–53 (2014).
41. Louwet, F., Groenendaal, L. & Dhaen, J. PEDOT/PSS: synthesis, characterization, properties and applications. *Synth. Met.* **135**, 115–117 (2003).
42. Ouyang, J., Chu, C.-W., Chen, F.-C., Xu, Q. & Yang, Y. High-Conductivity Poly(3,4-ethylenedioxythiophene):Poly(styrene sulfonate) Film and Its Application in Polymer Optoelectronic Devices. *Adv. Funct. Mater.* **15**, 203–208 (2005).
43. WANG, G., TAO, X. & WANG, R. Fabrication and characterization of OLEDs using PEDOT:PSS and MWCNT nanocomposites. *Compos. Sci. Technol.* **68**,

- 2837–2841 (2008).
44. Ely, F. *et al.* Patterning quality control of inkjet printed PEDOT:PSS films by wetting properties. *Synth. Met.* **161**, 2129–2134 (2011).
 45. Farinhas, J. *et al.* Nanostructured donor/acceptor interfaces in photovoltaic cells using columnar-grain films of a cross-linked poly(fluorene-alt-bithiophene). *J. Mater. Chem.* **21**, 12511 (2011).
 46. Ouyang, J. Solution-processed PEDOT:PSS films with conductivities as indium tin oxide through a treatment with mild and weak organic acids. *ACS Appl. Mater. Interfaces* **5**, 13082–8 (2013).
 47. Villers, D., Jobin, D. & Soucy, C. The influence of the range of electroactivity and capacitance of conducting polymers on the performance of carbon conducting polymer hybrid supercapacitor. *J. Electrochem. Soc.* **150**, A747–A752 (2003).
 48. Sun, K. *et al.* Review on application of PEDOTs and PEDOT:PSS in energy conversion and storage devices. *J. Mater. Sci. Mater. Electron.* **26**, 4438–4462 (2015).
 49. Lefebvre, M., Qi, Z. & Pickup, P. Electronically conducting proton exchange polymers as catalyst supports for proton exchange membrane fuel cells. Electrocatalysis of oxygen reduction, hydrogen. *J. Electrochem. Soc.* **146**, 2054–58 (1999).
 50. Lipomi, D. & Tee, B. Stretchable organic solar cells. *Adv. Mater.* **23**, 1771–75 (2011).
 51. Vosgueritchian, M. Highly conductive and transparent PEDOT: PSS films with a fluorosurfactant for stretchable and flexible transparent electrodes. *Adv. Funct. Mater.* **22**, 421–428 (2012).
 52. Luo, S.-C. *et al.* Poly(3,4-ethylenedioxythiophene) (PEDOT) nanobiointerfaces: thin, ultrasmooth, and functionalized PEDOT films with in vitro and in vivo biocompatibility. *Langmuir* **24**, 8071–7 (2008).
 53. Berezhetska, O., Liberelle, B., De Crescenzo, G. & Cicoira, F. A simple approach for protein covalent grafting on conducting polymer films. *J. Mater. Chem. B* **3**, 5087–5094 (2015).
 54. t-glase Features - taulman 3D. at <<http://www.aulman3d.com/t-glase-features.html>> (accessed October 28, 2015).
 55. Conductive PLA – ProtoPlant, Makers of Proto-pasta. at <<http://www.proto-pasta.com/pages/conductive-pla>> (accessed October 28, 2015).
 56. Liu, C. *et al.* Highly conducting free-standing poly(3,4-ethylenedioxythiophene)/poly(styrenesulfonate) films with improved thermoelectric performances. *Synth. Met.* **160**, 2481–2485 (2010).
 57. Yoo, J. E. *et al.* Directly patternable, highly conducting polymers for broad applications in organic electronics. *Proc. Natl. Acad. Sci. U. S. A.* **107**, 5712–7 (2010).
 58. Filament Tolerances and Print Quality. at <<http://www.protoparadigm.com/news-updates/filament-tolerances-and-print-quality/>> (accessed November 3, 2015).
 59. Su, Z., Li, Q., Liu, Y., Guo, W. & Wu, C. The nucleation effect of modified carbon black on crystallization of poly(lactic acid). *Polym. Eng. Sci.* **50**, 1658–1666 (2010).
 60. Cho, C.-K. *et al.* Mechanical flexibility of transparent PEDOT:PSS electrodes prepared by gravure printing for flexible organic solar cells. *Sol. Energy Mater. Sol. Cells* **95**, 3269–3275 (2011).
 61. Savagatrup, S. *et al.* Plasticization of PEDOT:PSS by Common Additives for Mechanically Robust Organic Solar Cells and Wearable Sensors. *Adv. Funct. Mater.* **25**, 427–436 (2015).
 62. Dráberová, E. *et al.* Class III beta-tubulin is constitutively coexpressed with glial fibrillary acidic protein and nestin in midgestational human fetal astrocytes: implications for phenotypic identity. *J. Neuropathol. Exp. Neurol.* **67**, 341–54 (2008).
 63. Donato, R. *et al.* Differential development of neuronal physiological responsiveness in two human neural stem cell lines. *BMC Neurosci.* **8**, 36 (2007).
 64. Chia, H. & Wu, B. Recent advances in 3D printing of biomaterials. *J. Biol. Eng.* **9**, 4 (2014).
 65. Lee, V. K. *et al.* in *Bioprinting Regen. Med.* (Turksen, K.) (Springer International Publishing, 2015). doi:10.1007/978-3-319-21386-6
 66. Nishiyama, Y. *et al.* Development of a three-dimensional bioprinter: construction of cell supporting structures using hydrogel and state-of-the-art inkjet technology. *J. Biomech. Eng.* **131**, 035001 (2009).